Engineering Geology 243 (2018) 282–293

Contents lists available at ScienceDirect

Engineering Geology

journal homepage: www.elsevier.com/locate/enggeo

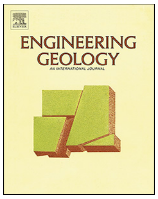

Integrated geophysical survey in a sinkhole-prone area: Microgravity, electrical resistivity tomographies, and seismic noise measurements to delimit its extension

Veronica Pazzi[a,*], Michele Di Filippo[b], Maria Di Nezza[c], Tommaso Carlà[a], Federica Bardi[a], Federico Marini[a,d], Katia Fontanelli[a], Emanuele Intrieri[a], Riccardo Fanti[a]

[a] *Department of Earth Sciences, University of Firenze, Via G. La Pira 4, 50121 Firenze, Italy*
[b] *Department of Earth Sciences, University of La Sapienza, Piazzale Aldo Moro 5, 00142 Roma, Italy*
[c] *National Institute of Geophysics and Volcanology, Via di Vigna Murata, 605, 00143 Roma, Italy*
[d] *Regional Doctoral School of Earth Sciences, University of Firenze, Via G. La Pira 4, 50121 Firenze, Italy*

ARTICLE INFO

Keywords:
Microgravity
3D electrical tomography
H/V method
Integrated geophysical approach
Sinkhole hazard

ABSTRACT

Detection, forecasting, early warning, and effective monitoring are key aspects for the delimitation of sinkhole-prone areas and for susceptibility assessment and risk mitigation. To attain these goals, direct and indirect techniques can be employed, and the integration of different indirect/non-invasive geophysical methods including 2D- and 3D-electrical resistivity tomography, microgravity, and single-station seismic noise measures was carried out at “Il Piano” (Elba Island – Italy), where at least nine sinkholes occurred between 2008 and 2014. The most likely origin for these sinkholes had been considered related to net erosion of sediment from the alluvium, caused by downward water circulation between the aquifer hosted in the upper layer (Quaternary alluvial deposits) and that in the lower (Triassic brecciated dolomitic limestone and Cretaceous slate). The integrated geophysical survey, therefore, was carried out a) to differentiate shallower from deeper geological layers, b) to detect possible cavities that could evolve into sinkholes, c) to suggest possible triggers, and d) to delimit the sinkhole-prone area. The results of the integrated geophysical surveys suggest that the study area is mainly characterised by paleochannels, and that the sinkhole-prone area boundaries correspond to these paleochannels.

1. Introduction

The term “sinkhole” was first introduced in the late sixties to indicate the subcircular surface depressions or collapse structures formed by the collapse of small subterranean karst cavities. Currently, sinkholes are related to subterranean cavities propagating up to the surface, regardless of their trigger and shape. According to the USGS (http://water.usgs.gov/edu/sinkholes.html) and the scientific literature (Guerrero et al., 2004; Waltham et al., 2005; Kaufmann, 2014; Argentieri et al., 2015; Sevil et al., 2017), sinkholes can be classified according to a large variety of schemes depending on the dominant process of formation and on the geological scenario behind the development of the phenomenon. Specifically, three main factors can be identified: i) predisposing causes, such as the nature of the sub-superficial geology and the bedrock and the presence of sub-superficial anthropogenic structures; ii) triggering causes, such as rain or the superficial drainage of water infiltrating into the soil; and iii) concurrent causes, such as the anthropic effect on the continuity of the superficial drainage network and the extraction of superficial water.

Sinkholes can cause spatially dispersed damage. In particular, related losses are direct (e.g., human casualties and damage to property), indirect (e.g., interruption to businesses, transport infrastructure and communication networks) and intangible, especially if they occur in urban areas (Galve et al., 2012; Intrieri et al., 2015; Sevil et al., 2017). Knowing the formation mechanism, some general actions may be identified as countermeasures to mitigate the sinkhole susceptibility of the area and to overcome the environmental and infrastructure problems. In addition, considering that in general, sinkholes are densely clustered in “sinkhole-prone areas” while completely absent in others, key aspects of sinkhole risk mitigation are setting up early warning systems on the basis of effective monitoring programmes (to predict where and when new phenomena will occur) and assessing how

---

[*] Corresponding author.
E-mail address: veronica.pazzi@unifi.it (V. Pazzi).

https://doi.org/10.1016/j.enggeo.2018.07.016
Received 18 September 2017; Received in revised form 4 May 2018; Accepted 17 July 2018

existing systems will evolve (Guerrero et al., 2004; Kaufmann, 2014). However, techniques developed specifically for sinkhole detection, forecasting and monitoring are missing, probably because of a general lack of sinkhole risk awareness and of the intrinsic difficulties involved in detecting precursory sinkhole deformations before collapse (Intrieri et al., 2015). Therefore, direct and indirect techniques able at least to detect existing subterranean cavities are important. Among the direct methods, blind drillings in sinkhole-prone areas and electric cone penetration tests (CPT) are common applications; nevertheless, these methods puncture the surface, may be disadvantageous in urban areas and may exacerbate sinkhole development (Zhou et al., 2002; Krawczyk et al., 2012; Samyn et al., 2014; Lee et al., 2016; Sevil et al., 2017). On the other hand, indirect techniques allow for the extrapolation of data concerning sinkhole location and risk by means of a) the back-analysis of past events, b) the stratigraphy of the sediments filling existing sinkholes, and c) the susceptibility models generated by analysing the statistical relationship between the spatial distribution of sinkholes and that of specific conditioning factors (Pueyo Anchuela et al., 2013; Kaufmann, 2014; Zini et al., 2015).

Currently, non-invasive high-resolution geophysical methods for shallow exploration and imaging of local subsurface heterogeneities are recognised as the best practice approaches to identify and map sinkholes, especially if they are actively developing (Smith, 1986; Zhou et al., 2002; Ezersky, 2008; Krawczyk et al., 2012; Martinez-Moreno et al., 2013; Pueyo Anchuela et al., 2013; Cardarelli et al., 2014; Kaufmann, 2014; Samyn et al., 2014; Argentieri et al., 2015; Zini et al., 2015). Natural cavities, in fact, can be filled with air, water, or collapsed/unconsolidated material, resulting in variations in the ground physical properties and therefore providing fairly distinct geophysical contrasts, which may be detected (Bishop et al., 1997). Moreover, since the rock surrounding the cavity is often disturbed, the associated fracturing may extend up to two or more diameters away from the cavity.

In this paper, we present the results of an integrated geophysical survey at “Il Piano” (meaning “Flat” in Italian, Elba Island – Italy), where at least nine sinkholes occurred between 2008 and 2014 (Intrieri et al., 2015), with the aims of a) obtaining a suitable geological and hydrogeological model of the area, b) detecting possible cavities that could evolve in sinkholes, c) suggesting possible triggers, and d) delimiting the sinkhole-prone area. The most likely origin for these sinkholes has been considered related to net erosion of sediment from the alluvium caused by downward water circulation between the superficial aquifer and the main karst aquifer represented by the local rock substratum (Intrieri et al., 2015). Therefore, to differentiate shallower (Quaternary alluvial deposits) from deeper (Triassic brecciated dolomitic limestone and Cretaceous slate) geological layers and to detect possible cavities in the karst bedrock, investigations by means of 2D- and 3D-electrical resistivity tomography (ERT), microgravity, and single-station seismic noise measurements (H/V) were carried out. This integrated geophysical approach is included in a wider project (Fig. 1) aimed at characterising the geomorphology and hydrogeology of the area (Intrieri et al., 2018). The key result of this study is that the hazards of the area are ascribable to shallow causes (i.e., water infiltrating into the soil and related fine material transport) instead of deeper ones (i.e., karst caves).

The paper is structured as follows: Section 2 provides a geological and geomorphological description of the study area; Section 3 details a brief overview of the employed techniques and methodology; Section 4 presents the results of the geophysical survey independently for each technique, while in Section 5, the overall data are integrated and discussed.

2. Study area

The complex Elba Island stack of nappes is identified as the westernmost part of the Northern Apennine chain (Bortolotti et al., 2001). From a geological point of view, the western part of the island is dominated by a large granodiorite pluton (Monte Capanne), whereas the eastern part is composed of a set of Ligurian and Tuscan tectonic units, mostly composed of sedimentary formations and Messinian-Pliocene intrusive magmatic bodies (Ferrara and Tonarini, 1985; Rocchi et al., 2002; Maineri et al., 2003). Bortolotti et al. (2001) provided an updated model of the structure of central and eastern Elba Island and defined nine, generally east-vergent, different tectonic complexes.

The study area is located in the northeastern part of the island (Fig. 2a) and corresponds to the mostly flat terrain separating the municipalities of Rio nell'Elba and Rio Marina. The most recent 1:25000 geologic map by ISPRA (http://sgi1.isprambiente.it/website/isolaelbageo/carta_geologica_isola_elba.htm) is dated 2015 and shows that the Cavo Formation (FCV in Fig. 2c, d) and the Rialbano Breccia (RBC in Fig. 2c, d), previously known as Calcare Cavernoso (Bortolotti et al., 2001; Intrieri et al., 2015), constitute the rock substrata herein. The Cavo Formation, a metamorphosed siltstone characterised by polyschistose calc-schists and varicoloured slates, tectonically overlies, by means of a N—S oriented, W-dipping fault, the Rialbano Breccia, a brecciated dolomitic limestone (Bortolotti et al., 2001). In the easternmost portion of the study area, the substratum consists of the Verrucano sequence, a HP-LT metamorphic sedimentary sequence. This substratum is extensively covered by approximately 20–30 m of alluvial (b in Fig. 2c, d) and erosional (a in Fig. 2c) deposits (Quaternary alluvium) composed of lenticular gravel and sand bodies within a sandy silt matrix. For a detailed lithologic description of these formations, see Bortolotti et al. (2001).

From a hydrogeological point of view, the outcropping formations are quite different: the Rialbano Breccia shows high permeability, mainly owing to tectonic fracturing and karst phenomena, while the permeability of the Cavo Formation metasiltstone is very low. The hydrographic basin is characterised by a narrow topography that separates “Il Piano” by means of the downhill end section from the outlet into the sea. This topography is the result of the geological and geomorphological evolution of the area, which reached its present appearance because of the fluctuations in sea level and the alternation of depositional and erosional events that occurred in the late Pleistocene and Holocene epochs (Bortolotti et al., 2001). Consequently, the area was gradually filled with continental deposits (i.e., of lacustrine, fluvial, hillslope, and mass transport origin). In the study area, two main aquifers can be recognised: a superficial one hosted by the Quaternary alluvium and the main one of karst origin hosted in the fractured limestone and deeply exploited for industrial, agricultural, and drinking purposes (Intrieri et al., 2015). The presence of water in the area is also witnessed by the past presence of at least 22 watermills, many millponds, and ditches for their hydraulic energy supply, the ruins of which are still largely visible (although in different states of preservation).

3. Material and methods

To detect caves, gravity and/or electrical methods were mainly employed and combined with other techniques (Martinez-Moreno et al., 2013). The integration of microgravity, ERT, and H/V technique was performed to characterise the study area and delineate the sinkhole-prone area (Fig. 3). Direct information about the subsoil properties was obtained from the Lefranc permeability test, SPTs, and stratigraphy boreholes carried out along the road SP26 (Fig. 2b, c) after the sinkholes developed in 2013. The microgravity surveys were conducted mostly in the inhabited areas around houses and along the two main roadways (Fig. 3). On the other hand, H/V measurements and ERT were carried out to characterise a wider area, although their distribution was influenced by field accessibility.

3.1. 2D- and 3D-ERT

To achieve the aims of this work, eight 2D- and seventeen 3D-ERT

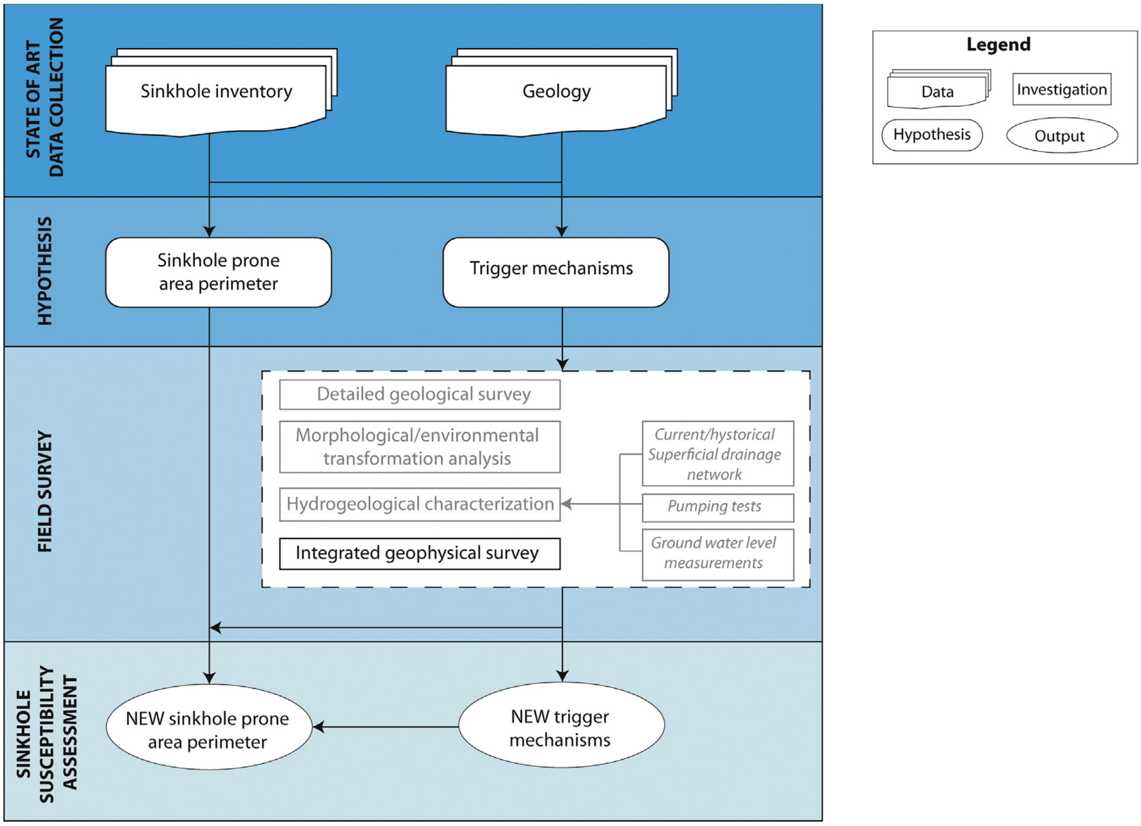

Fig. 1. Flow chart of the whole project: in black are the steps described in this paper; in grey are the steps that aim to characterise the geomorphology and hydrogeology of the area illustrated in detail in Intrieri et al., 2018.

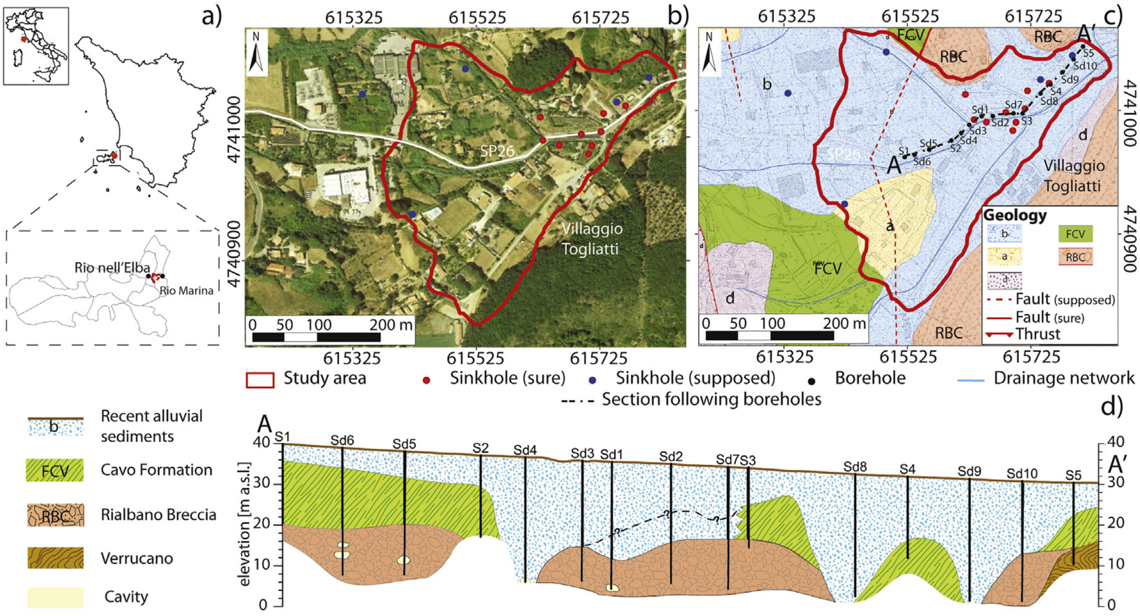

Fig. 2. a) Location of the study area with respect to the Tuscany Region and the municipalities of Rio nell'Elba and Rio Marina; b) satellite view of the study area; c) detailed geologic map (modified after Intrieri et al., 2015): the AA' section, which follows the borehole locations, is shown in d); d) geological section (AA' in c) derived from borehole surveys. In b) and c), the red line delimits the study area, the red and blue dots are verified and supposed sinkholes, respectively, and the white line marks the provincial road "SP26". In c), the black dots identify the boreholes while the blue lines denote the drainage network. Moreover, in c), "a" represents terraced alluvial sediments; "b", recent alluvial sediments; and "d", eluvial and colluvial debris. (For interpretation of the references to colour in this figure legend, the reader is referred to the web version of this article.)

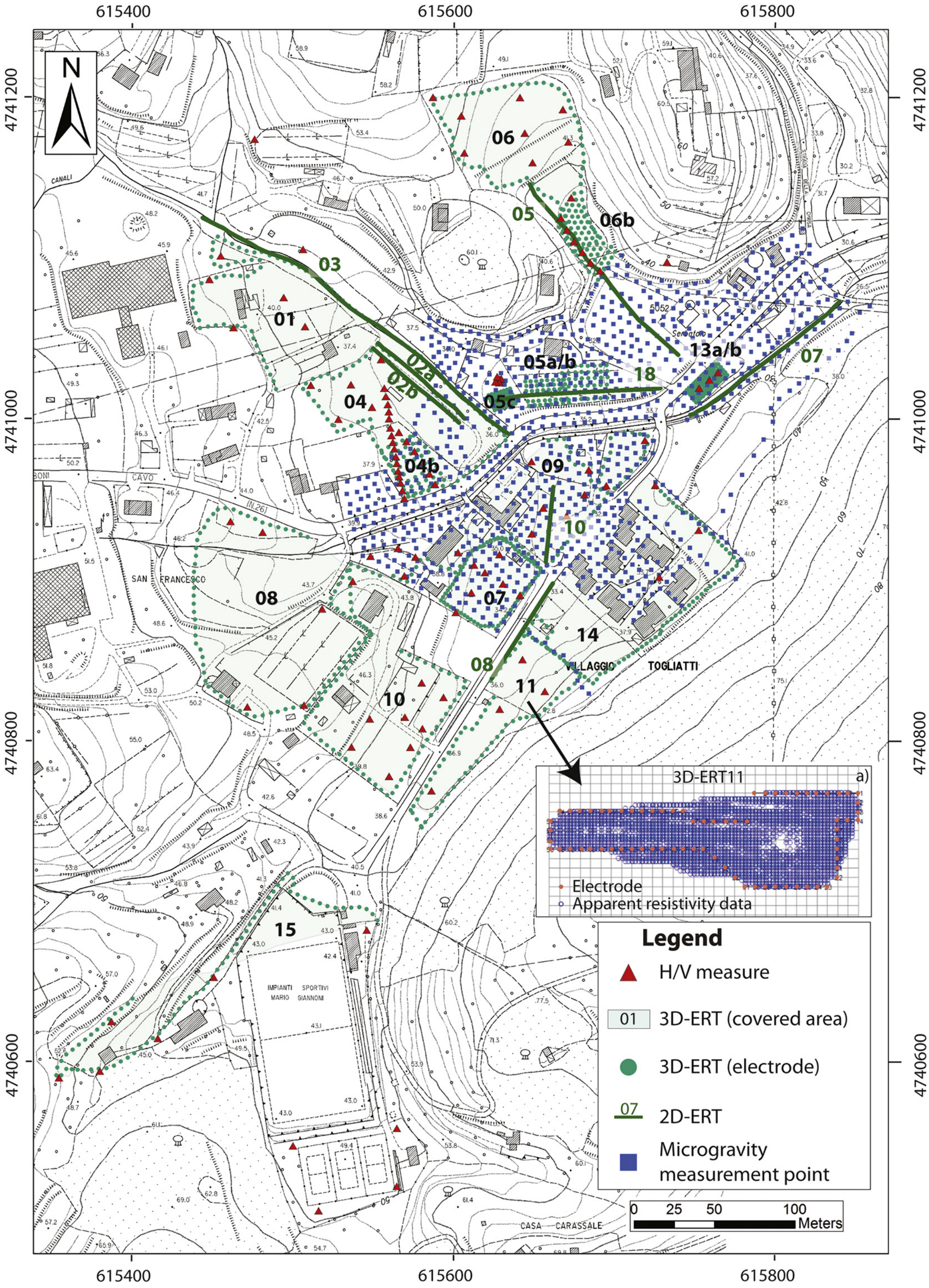

Fig. 3. Details of the geophysical campaign at “Il Piano”: H/V single-station seismic noise measures (red triangles), microgravity measures (blue squares), 2D-ERT (green lines), and 3D-ERT (the green dots mark the location of the electrodes, while the light green areas delimit the extension of the areas effectively investigated). In a) is shown, as an example, the 3D distribution of the acquired quadripoles (blue dots) for the 3D-ERT11 survey (the green dots mark the location of the electrodes). (For interpretation of the references to colour in this figure legend, the reader is referred to the web version of this article.)

were carried out at “Il Piano” (Fig. 3). The spatial distribution of the underground electrical resistivity, in fact, can provide useful information to characterise subsoil anomalies of both geological and human-made origin (Smith, 1986; Zhou et al., 2002; Santarato et al., 2011; Pazzi et al., 2016c). These ERT data were collected by means of a SyscalPro georesistivimeter (IRIS Instrument), coupled with either two or three multichannel cables with 24 channels (i.e., forty-eight or seventy-two electrodes, respectively), with a maximum electrode spacing of 5 m (Table 1). The electrodes were standard stainless-steel stakes. The pole-dipole array was employed for both 2D- and 3D-ERT measurements, as it combines consistent signal strength with good resolution and depth of investigation (Smith, 1986; Zhou et al., 2002; Samyn et al., 2014). Moreover, to collect 2D-ERT data as well, the dipole-dipole and Wenner-Schlumberger reciprocal arrays were used, the

Table 1
2D- and 3D-ERT: ERT name, inter-electrode distance, 2D-ERT total length or 3D-ERT area investigated, total number of acquired measures, percentage of removed data, and total number of iterations needed to obtain a converging model (a model with a small enough misfit between field and modelled data, Santarato et al., 2011).

	Name	Electrode spacing [m]	2D-total length [m]/3D-total area [m^2]	Acquired data [adim]	Removed data [%]	Iteration number [adim]
2D-ERT	02a	1.5	70.50	3054	6.4	5
	02b	1.5	70.50	3054	4.9	3
	03	5.0	235.00	3054	37.0	6
	05	3.0	141.00	3054	10.9	3
	07	2.5	117.50	3054	21.2	3
	08	1.5	70.50	3054	11.0	4
	10	1.0	47.00	3054	21.0	4
	18	2.2	103.40	3054	3.9	3
3D-ERT	01	5.0	6024.60	9616	17.3	8
	04	5.0	5707.43	9507	16.2	8
	04b	5.0	822.90	2058	7.0	7
	05a	4.0	585.90	2058	8.2	4
	05b	4.0	377.20	2058	8.2	4
	05c	2.0	140.30	2058	5.9	4
	06	2.5	819.10	3160	9.2	7
	06b	5.0	5321.80	8889	25.3	7
	07	2.5	2010.10	3770	8.5	6
	08	5.0	10,188.90	11,303	19.0	7
	09	5.0	5817.60	11,303	14.7	6
	10	5.0	6852.30	6868	23.4	7
	11	5.0	3123.20	8828	11.1	7
	13a	2.0	141.70	2058	7.8	4
	13b	2.0	152.70	2058	7.8	4
	14	3.5	8051.50	8281	11.2	8
	15	5.0	4135.70	8206	16.1	4

first to enhance the lateral resolution at shallow depth and the second to increase the depth of investigation and to take advantage of the instrument multichannel acquisition system (Santarato et al., 2011). The 3D-ERT acquisition sequences, which allow collecting data not only above the electrodes but also in the volume surrounded by the electrodes (Fig. 3a), were optimised for each ERT on the basis of the electrode geometry (Santarato et al., 2011; Viero et al., 2015): this procedure resulted in a variable number of acquired data during each measurement campaign (Table 1). All the electrodes were georeferred using a Leica 1200 differential GPS (mean 3D coordinate quality of 2.0 cm) in Real Time Kinematic mode (Pazzi et al., 2016b), and detailed terrestrial topographic surveys of the surrounding areas were performed to optimise the inversion procedure.

ERT inversions were carried out by the commercial software ErtLab© (Geostudi Astier S.r.l., Multi-Phase Technologies LLC) that implements Occam's regularisation to optimally manage data noise (Santarato et al., 2011; Viero et al., 2015). To remove outliers, i) the measures quality, ii) the voltage, iii) the current intensity, iv) the geometric factor, and v) the apparent resistivity distribution of each dataset was statistically analysed (i.e., the software calculated the frequency distribution of the analysed parameters), and the extreme tails of each distribution were thus removed. The iterative procedure needed to solve the inverse problem necessitated having an initial hypothesis, i.e., an apparent resistivity value for the starting homogeneous half-space. This initial value was chosen as the mean apparent resistivity value, or the value with the highest count in the histogram distribution (Viero et al., 2015). All the ERT inversions converged, meaning that the resistivity models of the last inversion had a residual value lower than the misfit function between the field and modelled data, as defined in Santarato et al. (2011).

3.2. Microgravity

The microgravity technique is effective to detect areas of contrasting or anomalous density by measuring the variation of the gravitational acceleration of the Earth. Currently, this method is still employed even though it is not cost-effective as a result of the large amount of fieldwork and number of post-processing corrections required. A LaCoste & Romberg model D gravimeter with a sensitivity of 5 μGal was used for microgravity observations in the study area. The station elevations were measured with a total station model Pentax R125N reflector Rless with an accuracy of 5–10 mm in horizontal and vertical coordinates. The gravity was estimated with respect to the gravity branch of Santa Barbara church in Rio Marina village and the elevation measurements of IGM (Italian Military Geographic Institute) benchmark n. 126,902 of San Pietro church in Rio nell'Elba. Gravity readings repeated on four control stations provided a root-mean-square error of $<$ 5 μGal. The Santa Barbara Church base point was selected in the area, and all the gravity measurements were referenced to this point. This local microgravity network was linked to the S. Angelo Romano Absolute Gravity Station (D'Agostino et al., 2008) located on Meso-Cenozoic carbonate rocks of Mt. Cornicolani close to Rome. The microgravity survey consisted of 964 measurement points spaced in a grid of 6 m to 8 m. The observed gravity data are the sum of gravity fields produced by all underground sources. The targets for these specific surveys are often small-scale structures buried at shallow depths, and these targets are embedded in a regional field that arises from residual sources that are usually larger or deeper than the targets or are located farther away. Correct estimation and removal of the regional field from the initial field observations yields the residual field produced by the target sources. Therefore, to detect the deeper regional geological trend, to improve the coverage, and to obtain more precise contours in the eastern part of the island, an additional gravity survey was conducted. Sixty gravity stations were established and used to compute the Bouguer anomalies. The locations of the stations were obtained using differential GPS measurements.

The microgravity and gravity anomalies were computed with reference to the 1980 ellipsoid (Moritz, 1984). Density values of 2150 kg/m^3 (Quaternary alluvial deposits) and 2650 kg/m^3 (deeper geological bedrock: Cavo Formation and Rialbano Breccia) were used for the Bouguer anomaly computation and the terrain effects, respectively. These density values were estimated by laboratory measurements on rocks sampled in the study area and by means of analytical or graphical methods such as those proposed by Nettleton (1942). The terrain correction was the most sensitive stage among the different gravity reductions because of the rough topography of the study area (Regional Technical Map, CTR 1:10000; bathymetric survey). After applying Earth tide, free-air and Bouguer corrections, the Bouguer gravity anomalies were computed. The evaluation of the accuracy of gravity anomalies included estimation of measurement precision and of the errors in anomaly calculations. Most of the uncertainty components in the Bouguer anomaly accuracy estimations were negligible in comparison with the terrain correction component. The final microgravity and gravity Bouguer anomaly accuracies were here estimated at ± 0.005 mGal and ± 0.05 mGal, respectively.

The separation of the Bouguer gravity anomaly, i.e., the process of discerning local structures (residual gravity anomalies) from the regional gravity trend, was carried out using both the polynomial fitting approach and Griffin (1949). In the radial weights method (Griffin, 1949), the averaged values are those on the circumference of a circle centred at the station. Usually, the values are obtained by interpolation from the gravity map contours. The result slightly depends on the number of selected points, and even more on the radius of the circle. The radius is usually of the same order of magnitude as the depth of the anomaly to be emphasised, but both shallower and deeper anomalies still contribute to the results. The acquisition grid is generally approximately half the radius used for averaging. Six circles with different radii were used: 10 m, 15 m, 20 m, 30 m, 40 m, and 50 m. Finally, a three-dimensional model of the spatial distribution of the gravity anomalies was computed. This final model was a range of elementary gravity distributions used as the source of the anomalies (methods of Griffin, 1949).

3.3. *H/V measurement*

Passive seismic methods (Sgarlato et al., 2011; Samyn et al., 2014) are commonly employed to detect sinkholes. Among these, the horizontal to vertical spectral ratio (H/V) technique (Nakamura, 1989; SESAME, 2004; Del Gaudio et al., 2014) has proven to be one of the most appropriate methods to estimate the fundamental/resonance frequency of soft deposits, as well as to study the interactions between soil and buildings (Pazzi et al., 2016a, 2017a). Nowadays, the application of H/V measurement is also a challenge issue in mountainous areas (Pazzi et al., 2017b). The spectral features and polarisation of seismic noise, in fact, show strong correlations with the site geological setting (Lotti et al., 2015, 2017). To achieve the aims of this project, H/V measurements were carried out to characterise the alluvial sediment cover (Del Soldato et al., 2018). One hundred twenty single-station seismic noise traces were recorded at “Il Piano” by means of five Tromino®, the all-in-one compact 3-directional 24-bit digital tromometer developed by MoHo S.r.l. (1 dm^3 volume and 1 kg weight). The instrument-soil coupling was obtained by the pin set supplied with these instruments. Each acquisition was run for 30 min at 256 Hz. These instruments were chosen according to the SESAME (2004) owing to their i) simplicity of use, ii) compact size, and iii) absence of connection cables between geophones, seismographs and dataloggers, considerably reducing the noise induced by instrumentation on measures of seismic noise. For the ERT, all the single-station measures were georeferred using a Leica 1200 differential GPS (mean 3D coordinate quality of 2.0 cm) in Real Time Kinematic mode (Pazzi et al., 2016b).

The Grilla® software program (by MoHo S.r.l.) was used a) to analyse and process each single-station seismic noise acquisition, since it applies the SESAME (2004) standards and guidelines for processing ambient vibration data; b) to evaluate the directionality of each spectral peak; and c) to reconstruct the local seismic velocity profiles, constraining each acquisition with soil density and porosity values derived from the literature, and first-layer velocity measured as explained in Pazzi et al. (2017b). It is known, in fact, that the sedimentary layer thickness (h) and the layer shear velocity (Vs) in a single-layer stratigraphy are related to the H/V peak frequency (f) by means of the equation $f = \mathrm{Vs}/4\,h$. When no constraints are imposed, each H/V curve can be fitted by infinite synthetic models. In contrast, constraining the shallow subsoil stratigraphy or the first-layer Vs, it is possible to reconstruct the Vs profile, obtaining the thicknesses and velocity values of each layer (Castellaro, 2016). Finally, some alignments across the study area were defined, and single-station seismic noise acquisitions, acquired along each alignment, were elaborated to generate synthetic contour maps of the H/V (Pazzi et al., 2017b).

4. Results

4.1. *Geoelectrical results*

The 2D-ERT reached a mean depth of 20 m (minimum depth value: 8 m, 2D-ERT10; maximum depth value: 40 m, 2D-ERT03), while the mean depth of the 3D-ERT was approximately 30 m (minimum depth value: 3 m, 3D-ERT05c; maximum depth value: 40 m, 3D-ERT01). As already mentioned in Section 3, the ERT results were calibrated by means of the subsoil stratigraphies obtained from borehole logs carried out along the road SP26 (Fig. 2b, c). Fig. 2d shows the geological section, which follows the borehole locations, gathered from the boreholes themselves and employed to interpret the geophysical results. The area has a resistivity mean value in the range of 50–100 Ωm (green in Fig. 4), according to the resistivity range of the Quaternary alluvial deposits (b in Fig. 2). Saturated loose sand and/or clay levels, whose presence was found up to a depth of 30 m, appear as low-resistivity zones, characterised by resistivity values < 50 Ωm (cool colours, from dark to violet/white in Fig. 4). Gravel, dry sand or high-porosity materials containing voids appear to have high resistivity values, > 100 Ωm (green and yellow in Fig. 4) (Ezersky, 2008). Brecciated dolomitic limestones (Rialbano Breccia, 3DERT06-06b; RBC in Fig. 2) and very weathered metamorphosed siltstones (Cavo Formation, 3DERT15; FCV in Fig. 2) have resistivities > 150 Ωm (red in Fig. 4).

4.2. *Microgravity results*

Minima (negative anomalies) in microgravity data are caused by shallow low-density zones, such as cavities or soils with low compactness or high void ratios. The effective size of a gravity anomaly caused by a cavity is also dependent on the connectivity of cracks in its surroundings and on the genesis of the cavity in its host rock (Bishop et al., 1997). The Bouguer anomaly map (Fig. 5a) shows that the regional anomalies are quite dominant, especially in the west sector (Fig. 5a). In particular, the “Il Piano” study area (red line in Fig. 5a, enlarged in Fig. 5b) is characterised by an increasing trend from SW to NE (from 33.60 to 35.75 mGal, Fig. 5b). In this sector of the island, a strong gradient borders the area of microgravity surveying. The regional anomalies reflect the density, geometry and thickness variations of the regional basement and the lower crust. These anomalies have been computed using the third-order polynomial fitting method and removed from the Bouguer data to obtain residual anomalies to highlight local anomalies. The results are shown in Fig. 5c. Several relative negative anomalies (from green to dark blue/violet in Fig. 5c) are detected, mainly located in the eastern part of the microgravity survey area. A prevalently negative, oval-shaped residual anomaly characterised by a NE–SW trend is located in the northeast sector of the figure. Its minimum ranges from approximately −0.050 mGal to −0.100 mGal and is flanked by a positive anomaly of approximately +0.100 mGal (from yellow to red in Fig. 5c). The SP26 road (white dashed line in Fig. 5), which splits the surveyed area, is characterised in the western section by the alternation of negative and positive anomalies. Moreover, in correspondence with the dwellings of Villaggio Togliatti overlooking the road, there is a large subcircular negative gravity area up to −0.100 mGal. To estimate the maximum depth of these anomalies (Fig. 5c), the second-derivative Griffin (1949) with a 30-m radius has been calculated. In this method, the half-distance of upward continuation is considered as the depth of the downward continuation. Fig. 5d shows the results: several other negative anomalies are distinguishable, and they seem to branch from the main channel of negative anomalies.

4.3. *H/V results*

The distribution of the seismic noise single-station measures is shown in Fig. 3. It is well known that high-frequency peaks in the mean H/V curve are related to shallow depth interfaces and low-frequency H/V peaks to deep interfaces (Castellaro, 2016). In the whole dataset, at most three natural peaks may be identified (Fig. 6) that correspond to three different interfaces for which depths could be calculated as described in Section 3.3. These depths were obtained starting from a first-layer shear velocity value ranging from 100 m/s up to 250 m/s. The shallowest natural peak is in the range of 60–90 Hz and corresponds to the first discontinuity located at a depth of approximately 0.2–1.5 m, the second is in the frequency range of 12–30 Hz that corresponds to a discontinuity located at a depth of approximately 1.5–7.6 m, and the deepest is in the frequency range of 3.5–7.8 Hz that corresponds to a depth of approximately 10.5–35 m. These last values could also be interpreted as the thickness range of the valley replenishment material.

Since it is not possible to show here all the acquired traces, a

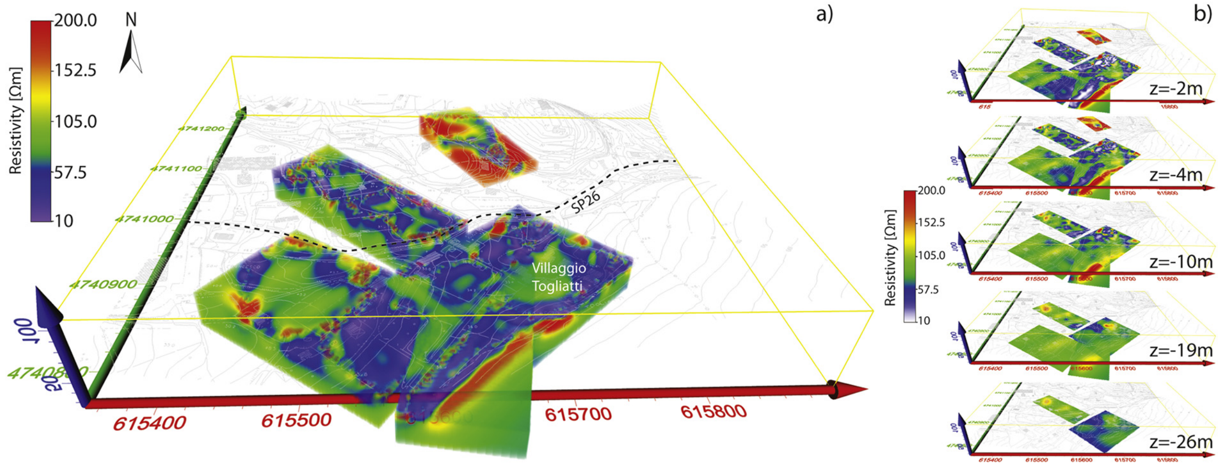

Fig. 4. a) 3D view (from south to north) of the geoelectrical results and b) 2D slice at different depths from ground level (from −2 m to −26 m). The black dashed line in a) is the SP26 road.

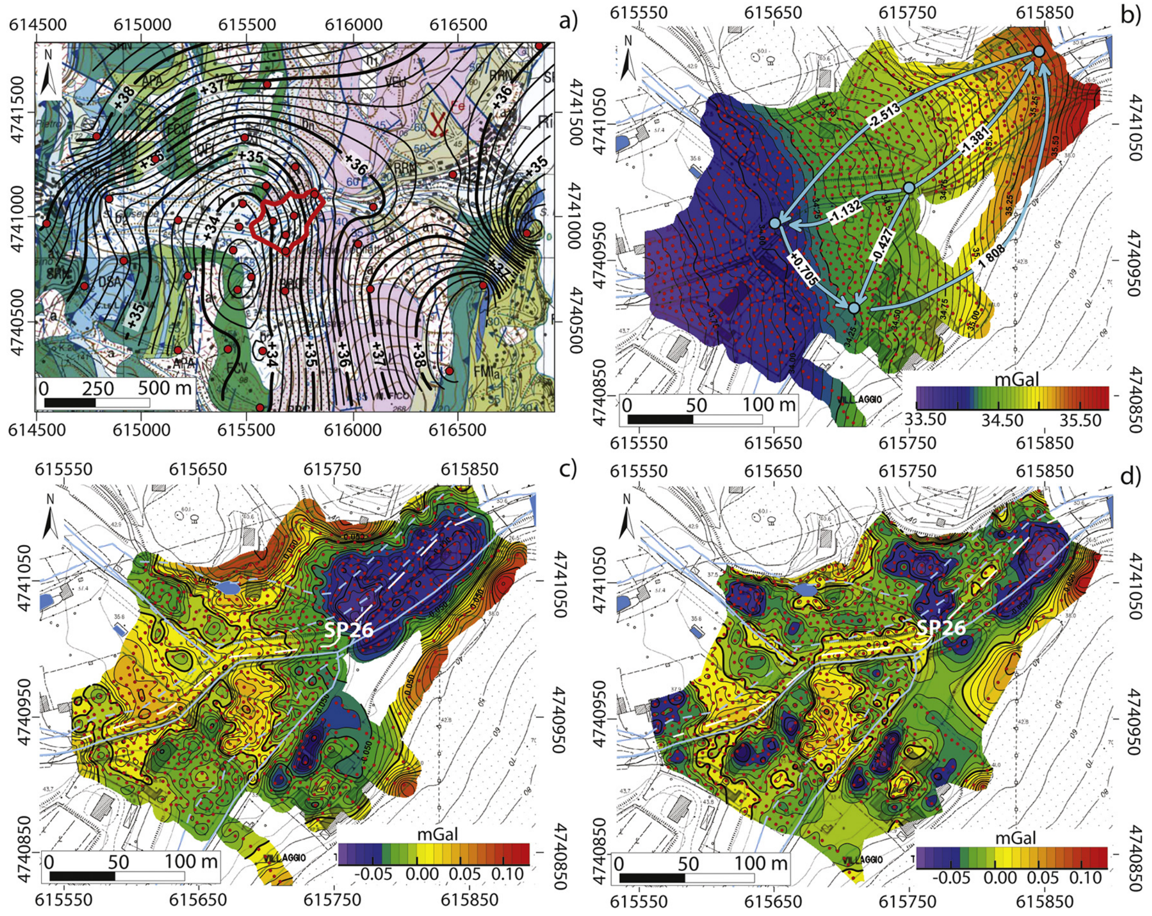

Fig. 5. a) Bouguer anomalies (mGal) of the eastern part of Elba Island overlaid on the geological map by ISPRA: the red line delimits the “Il Piano” microgravity survey area, while the red dots are some of the sixty gravity stations used as references to calculate the Bouguer anomaly. b) Bouguer anomalies (mGal) of “Il Piano” overlaid on the Regional Technical Map (CTR – 1:10000): the red dots indicate the locations of the gravity stations; the light blue dots, the control stations where measures were repeated to calculate the root-mean-square error; and the light blue arrows, the net gravity variation ΔG (mGal). c) Residual anomalies (mGal) calculated by a third-order polynomial fitting. d) Residual anomalies (mGal) using the second-derivative Griffin (1949) method with a 30-m radius. In both images: the white dashed line is the SP26 road, the light blue dashed lines are the old drainage network, while the solid ones the current, and finally the blue areas are millpond present in the Grand-ducal Land Registry. (For interpretation of the references to colour in this figure legend, the reader is referred to the web version of this article.)

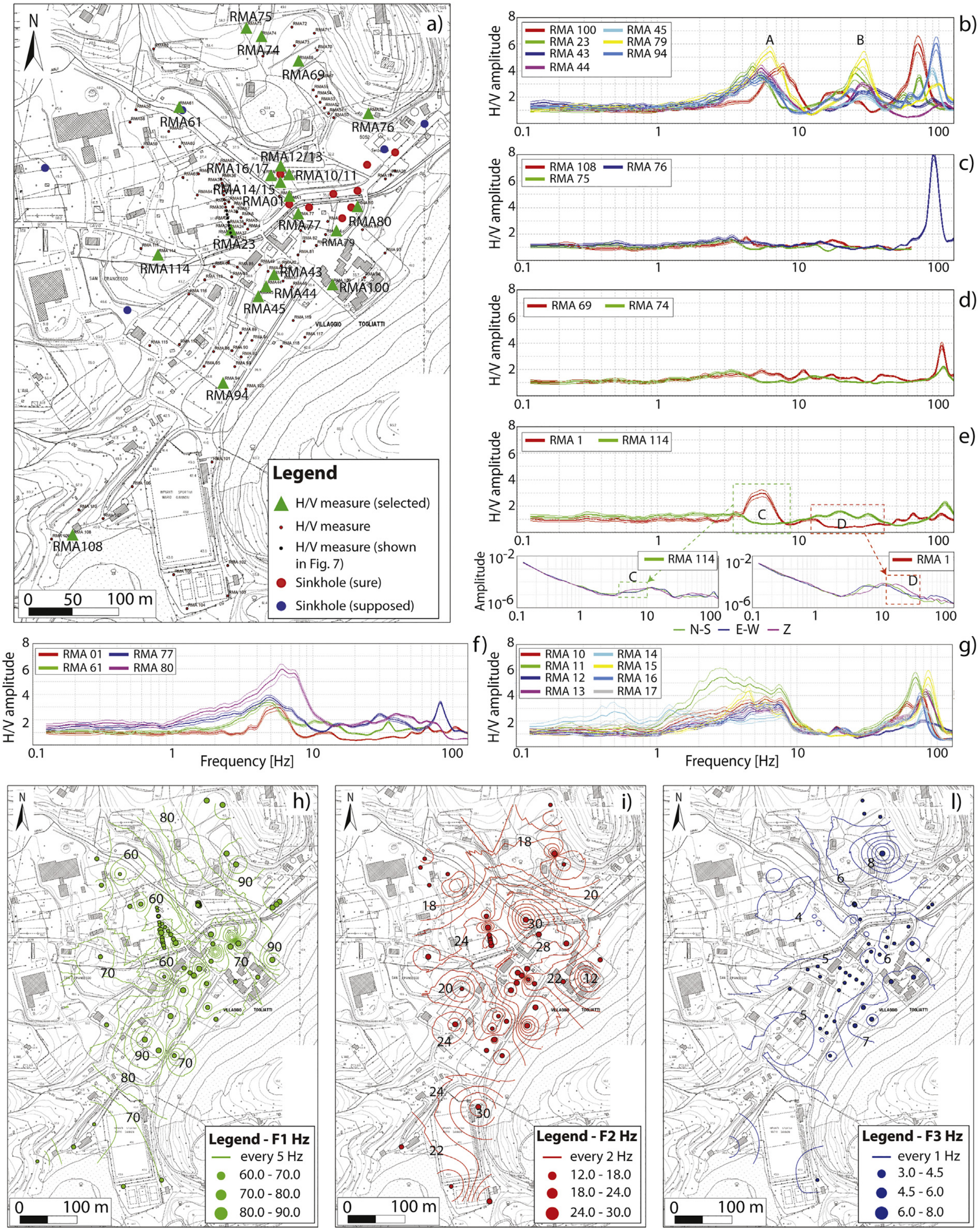

Fig. 6. Most significant H/V results: a) an overview map of the selected H/V single-station measures (green triangles) and of the verified (red dots) and supposed (blue dots) sinkholes. b) Traces with two natural peaks corresponding to the interfaces of siltstone/limestone (A, range 4–7 Hz) and alluvium/siltstone (B, range 20–30 Hz). c) Flat traces acquired on outcropping bedrock. d) Traces acquired on the outcropping bedrock, which show an amplification < 2. e) Traces with H/V amplitude < 1 associated with a velocity inversion (C and D are the spectra of these traces where the velocity inversion is clear). f) and g) Traces acquired beside/on verified or supposed sinkholes. Black dots in a) are the single-station measures selected to draw the H/V contour map shown in Fig. 7. (For interpretation of the references to colour in this figure legend, the reader is referred to the web version of this article.)

selection of the most significant results is displayed in Fig. 6 as follows: i) the RMA23, RMA43, RMA44, RMA45, RMA79, RMA94, and RMA100 traces (Fig. 6b), clearly showing the natural peaks (range 20–30 Hz) corresponding to the second (B in Fig. 6) and third interfaces (range 4–7 Hz, A in Fig. 6b); ii) the flat traces RMA75, RMA 76 and RMA108 (Fig. 6c), acquired on outcropping seismic bedrock (Castellaro, 2016; Pazzi et al., 2017b); iii) the RMA69 and RMA74 traces (Fig. 6d), acquired on nearly outcropping bedrock and depicting an

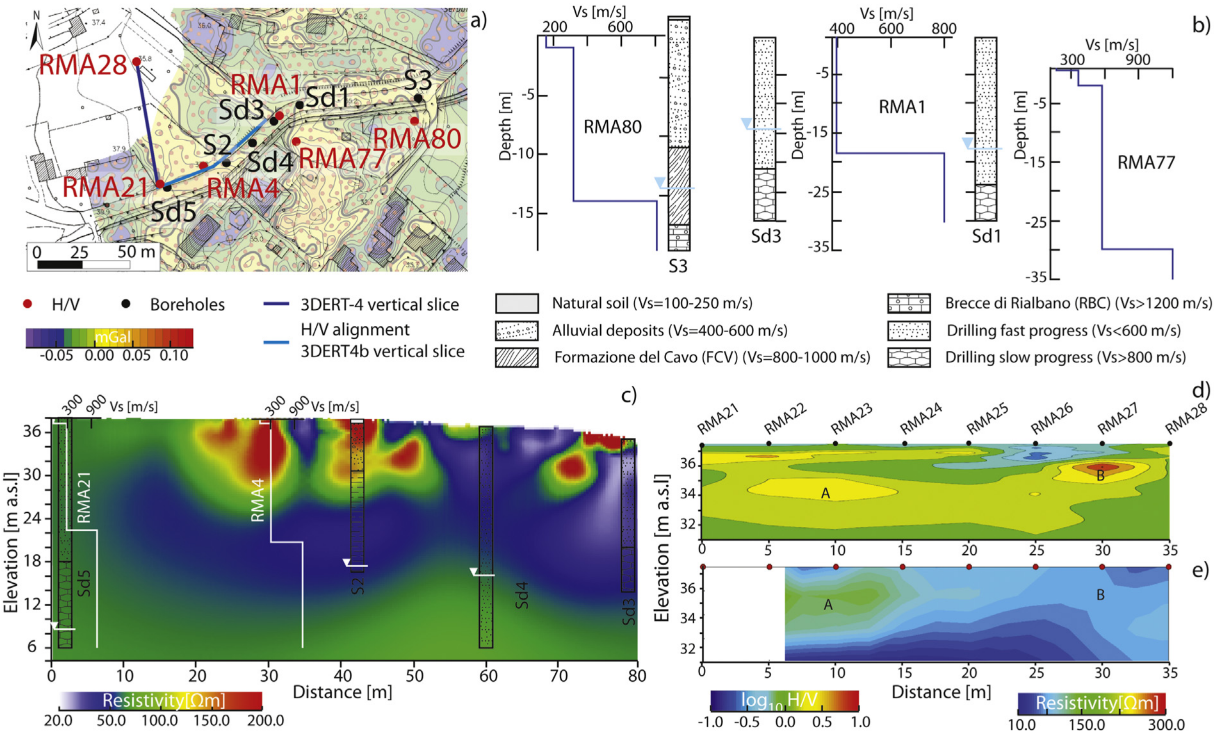

Fig. 7. a) Locations of the measurements employed for the qualitative comparison of the integrated geophysical survey data. Black dots are boreholes; red dots are H/V measurements; light blue line is the vertical slice extracted from 3DERT-4; blue line is the H/V alignment and the vertical slice extracted from 3DERT-4b. b) Comparison between boreholes and the Vs profiles derived from the fitting of the H/V measurements. c) Comparison between the Sd5, S2, Sd4, and Sd3 boreholes and the 3D-ERT-4 vertical slice carried out near the SP26 road. d) H/V contour map of the alignments RMA21–28 (black dots in Fig. 6). e) A parallel 2D vertical section extracted from the 3DERT0-4b. A and B are two lenticular gravel bodies characterised by positive seismic impedance contrasts and resistivity values higher than 80 Ωm. (For interpretation of the references to colour in this figure legend, the reader is referred to the web version of this article.)

amplification < 2 because of the very low seismic impedance contrast; iv) the RMA01 and RMA114 traces (Fig. 6e), showing a velocity inversion in the upper layers: the first (D in Fig. 6e) because it was acquired on asphalt (Castellaro, 2016) and the second (C in Fig. 6e) because of unspecified geological causes; and v) the H/V mean curves of the seismic noise traces acquired on or in proximity of the verified (RMA01, RMA10–17, RMA77, RMA80) or supposed (RMA61) sinkholes (Fig. 6f, g).

5. Discussion

The sinkholes at “Il Piano” (Elba Island, Italy) have represented a serious problem in the past years: at least nine sinkholes affected the area between 2008 and 2014 without any apparent triggering factor. Geophysical integrated investigations (2D- and 3D-electrical tomography, microgravity and H/V measurements) were performed in the area together with an accurate historical and hydrogeological reconstruction (Intrieri et al., 2018). The great amount of collected data was employed to extensively reconstruct the subsurface stratigraphy and to draw the boundaries of the sinkhole-prone area.

First, the information derived from the boreholes drilled after the 2013 sinkhole along the SP26 road was employed to qualitatively evaluate the microgravity anomalies, the resistivity values, and the Vs profiles derived from the fitting of the H/V curves (Fig. 7). Even thought the huge amount of acquired data and the high sensitivity of the whole dataset, the evaluation was qualitative and not quantitative because of the different precision in measuring data of each employed techniques. From the comparison between the boreholes (black dots in Fig. 7a) and the Vs profiles (red dots in Fig. 7a), a) the first discontinuity (frequency range of 60–90 Hz, depth of approximately 0.2–1.5 m) is between the anthropogenic altered layer and the Quaternary alluvial deposits; b) the second interface (frequency range of 12–30 Hz, depth of approximately 1.5–7.6 m) is between the alluvium and the locally weathered siltstones; and c) the deepest impedance contrast (frequency range of 3.5–7.8 Hz, depth of approximately 10.5–35 m) is between siltstones and brecciated dolomitic limestones (Rialbano Breccia). In Fig. 7c, the boreholes are compared with an electrical resistivity section extracted from 3DERT-4 (light blue line in Fig. 7a). It is possible to observe that the resistivity of the first layer (alluvial deposits) varies widely because of the extreme heterogeneity of the detrital material (Quaternary alluvium deposits) and also the saturation status. It is well known, in fact, that the resistivity is affected by the soil water content. According to Intrieri et al. (2018) the period October 2015 – June 2016 was quite dry, with respect to the rainfall seasonal mean values, and the piezometric level was constant. Therefore, the resistivity anomalies can be interpreted as an alternation of variable grain size deposits, characterised by heteropic facies, interdigitations and lenticular bodies of gravel and sand within a horizontal medium- to fine-grained layer with particle size increasing upwards. In the recent and Holocene epochs, in fact, the superficial streams deployed depositional and erosional material. These bodies and elements are highlighted at different depths by the geognostic and geophysical analysis as contrasts in the physical parameters, which may result in different rheological behaviour depending on various aspects (geotechnical, hydrological, hydraulic). Moreover, low-resistivity zones (< 50 Ωm, Fig. 4), located up to 30 m in depth and having a sinuous morphology, have been interpreted as old channels, mainly composed of saturated loose sand and clay levels.

Fig. 7 also shows the comparison between the alignment RMA21–28 (black dots in Fig. 6) and a parallel 2D section obtained from 3DERT-4b. In the H/V contour map (Fig. 7d), warm colours (from yellow to red) are associated with positive impedance contrasts ($\log_{10}$ H/V > 0), such as the contrast between the less saturated lenticular sand/gravel bodies (resistivity higher than 80 Ωm in Fig. 7e) and the sand/clay deposits

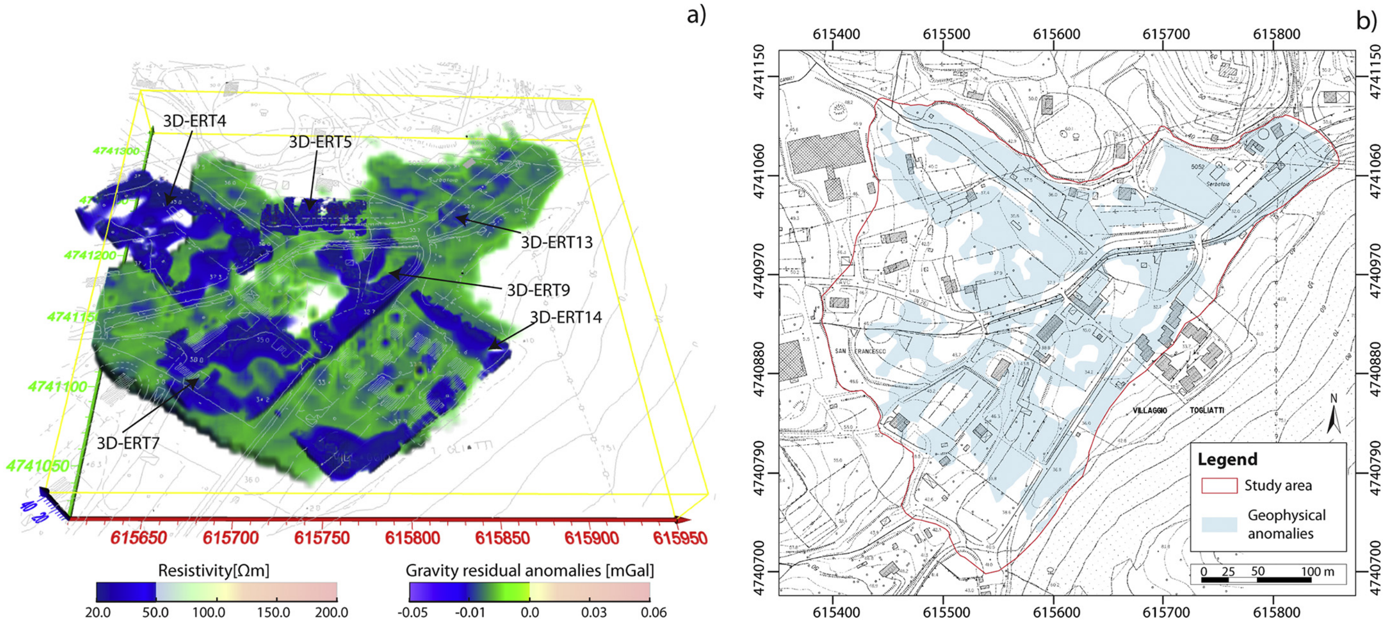

Fig. 8. a) Overlapping of the ERT and microgravity survey results. In the colour scales resistivity values > 50 Ωm and gravity positive values were turned white. b) 2D projection on the surface of the maximum lateral extension of the 3D interdigitations and lenticular bodies of gravel and sand within the horizontal medium- to fine-grained layer, highlighted at different depths by the integrated geophysical survey. This 2D projection does not take into account the bodies in depth distribution.

(resistivity lower than 80 Ωm in Fig. 7e). Cold colours (from light to dark blue in Fig. 7d) are associated with negative impedance contrasts ($\log_{10}$ H/V < 0) corresponding to velocity inversion in the uppermost layers. Green areas correspond to an absence of impedance contrast ($\log_{10}$ H/V = 0 in Fig. 7d) and therefore to an absence of seismic velocity variations between layers. Both electrical investigations and microgravity analyses reached a depth that was at least enough to identify the bedrock, while H/V measures allowed obtaining this information (the third interface, associated with the lowest natural peaks, located at a maximum depth of 35 m). In contrast, the H/V traces were not useful to identify sinkholes since the traces performed near verified sinkholes look qualitatively similar to the others as shown in Fig. 6b, f, and g.

The spatial distribution of gravity anomalies shows a complex geological setting; as the sources of microgravity anomalies are shallow minor geological structures, their effects are commonly between 0.010 and 0.040 mGal (from yellow to red in Fig. 5b). The main negative anomalies (dark blue/violet in Fig. 5b) correspond to the collapsed areas and expand towards the east. Negative anomaly zones indicate a mass depletion region, which may be associated with Quaternary alluvial deposits affected by sinkhole risk. The relative positive anomalies are associated with high density values (Cavo Formation, Rialbano Breccia). Finally, the negative zones are connected to each other by persistent subterranean channels within deposits of higher compactness (conglomerates). The negative anomalies are mainly located on or along riverbeds or near the pools of water accumulation when the various mills were active. Generally, the negative anomalies are in agreement with the hydraulic system of old natural waterways. However, these streams are superimposed upon another older hydrological system, which has been covered on the surface by the construction of the SP26 road. This hydrological system is still visible based on the location of the negative anomalies.

The overlapping between electrical tomographies and microgravity surveys (Fig. 8a) reveals that in correspondence with zones characterised by low resistivity values, the microgravity detected negative anomalies (dark blue/violet in Fig. 8a). These anomalies mainly correspond to old channels and pools that have been used in the past to provide water to mills. These mills have been progressively abandoned since the second half of the XX century and completely fallen into disuse in the first half of the 1990s; consequently, these channels have been abandoned. Indeed, sinkholes mainly occurred along these paleochannels. Nevertheless, an accurate 3D-delimitation of the paleochannel boundaries is not feasible. Fig. 8b shows the 2D projection on the surface of the maximum lateral extension of these 3D bodies, without considering their distribution in depth. This delimitation was qualitatively performed in a GIS environment. The horizontal 2D maps of the resistivity and microgravity anomalies at intervals of 1.0 m were imported. For each map, all the areas characterised by low resistivity values (< 50 Ωm) or a negative microgravity values were delimited. At the end, the maximum extensions of all these delimited areas were taken into account. This heterogeneity may be more marked in the easternmost portion of “Il Piano”, where the slope angle is reduced to zero and the water drained from the largest part of the whole “Il Piano” catchment basin converges.

This study represents an advancement with respect to the previous conceptual triggering model, according to which sinkholes were caused by the high hydraulic gradient in the first aquifer (possibly due to pumping), which produced erosion of fine particles (suffusion) that were drained within pre-existing subterranean cavities (Intrieri et al., 2015). Therefore, the first perimeter of the area susceptible to sinkholes was mostly based on the geology of the karst bedrock. Even though this trigger phenomenon cannot be completely excluded, the results of the integrated geophysical surveys indicate that no cavities are expected to be present in the bedrock. The microgravity survey, in fact, reveals no anomalies linkable to cavities of significant dimensions. The results of the hydrogeological survey evidence the presence of several ephemeral or intermittent streams, shallow water flows, and infiltrations (Intrieri et al., 2018). Moreover, they highlight that the sinkholes are mainly concentrated in a small area downstream and in the northern portion of the catchment basin (Intrieri et al., 2018). Therefore, the main cause of sinkhole formation in this area is not the dissolution of the karst bedrock but the sub-superficial water circulation in the aquifer hosted in the upper layer. This shallow circulation, in fact, during heavy rain events could be responsible to erode and transport fine sediments which removal produce macroscopic voids.

6. Conclusions

In an area where the most likely origin of sinkholes had been considered related to the erosion of sediments from the alluvium, the combined application of 2D- and 3D-ERT, microgravity, and H/V techniques was aimed at detecting possible cavities in the brecciated dolomite limestones, which could evolve into sinkholes, and therefore delimit the sinkhole-prone area. Among the results of the integrated geophysical survey are the following: a) the H/V method allows estimating the mean thickness of the alluvium, b) the 2D- and 3D-ERT permits characterising the electrical behaviour of the materials, and c) the microgravity provides suitable information on the spatial distribution of lower-density materials and does not detect significant cavities in the karst bedrock.

Overlapping the spatial distribution of the microgravity negative anomalies with the ERT values, it is possible to demonstrate that the lower-density masses are located in correspondence of the paleochannels that are mainly characterised by lenticular sand and gravel bodies within a sandy silt layer. It is also possible to draw the 2D projection of their maximum lateral extension on the surface, without considering their 3D distribution at depth. Despite the presence of karst bedrock, typically related to sinkhole formation, the integrated geophysical survey carried out in the study area permits dismissing the presence of cavities in the bedrock as the cause of the frequent collapses, and the main hazards of the area are ascribable to shallow causes (i.e., water infiltrating into the soil and related fine material transport).

Acknowledgments

This project was funded by the Municipality of Rio Marina together with the Municipality of Rio nell'Elba (grant number: Rep. 42/2015), thanks to Tuscany Region financing (grant number: Regional Council Resolution 319/2015). The authors would like to thank Niccolò Galfo, Lorenzo Giardi, and Gabriele Bicocchi for their fieldwork support and all the other people who helped them during the data collection, in addition to the inhabitants and the local authorities for their availability. The authors are also grateful to the anonymous reviewers and the Editor for their help improving the manuscript.

References

Argentieri, A., Carluccio, R., Cecchini, F., Chiappini, M., De Ritis, R., Di Filippo, M., Di Nezza, M., Marchetti, M., Margottini, S., Materni, V., Meloni, F., Nardi, A., Rotella, G., Sapia, V., Venuti, A., 2015. Early stage sinkhole formation in the Acque Albule basinof central Italy from geophysical and geochemical observation. Eng. Geol. 191, 36–47. https://doi.org/10.1016/j.enggeo.2015.03.010.

Bishop, I., Styles, P., Emsley, S.J., Ferguson, N.S., 1997. The Detection of Cavities Using the Microgravity Techniques: Case Histories from Mining and Karstic Environments. 12. Engineering Geology Special Publications, pp. 153–166. https://doi.org/10.1144/GSL.ENG.1997.012.01.13.

Bortolotti, V., Fazzuoli, M., Pandeli, E., Principi, G., Babbini, A., Corti, S., 2001. Geology of central and eastern Elba Island, Italy. Ofioliti 26 (2), 97–150.

Cardarelli, E., Cercato, M., De Donno, G., Di Filippo, G., 2014. Detection and imaging of piping sinkhole by integrated geophysical methods. Near Surf. Geophys. 12, 439–450.

Castellaro, S., 2016. The complementarity of H/V and dispersion curves. Geophysics 81, T323–T338. https://doi.org/10.1190/GEO2015-0399.1.

D'Agostino, G., Desogus, S., Germak, A., Origlia, C., Quagliotti, D., Berrino, G., Corrado, G., D'Errico, V., Ricciardi, G., 2008. The new IMGC-02 transportable absolute gravimeter: measurement apparatus and applications in geophysics and volcanology. Ann. Geophys. 51, 39–49.

Del Gaudio, V., Muscillo, S., Wasowski, J., 2014. What we can learn about slope response to earthquake from ambient noise analysis: an overview. Eng. Geol. 182, 182–200. https://doi.org/10.1016/j.enggeo.2014.05.010.

Del Soldato, M., Pazzi, V., Segoni, S., De Vita, P., Tofani, V., Moretti, S., 2018. Spatial modelling of depth to bedrock in peri-volcanic areas of Campania (southern Italy). Earth Surf. Process. https://doi.org/10.1002/esp.4350. (In Press).

Ezersky, M., 2008. Geoelectric structure of the Ein Gedi sinkhole occurrence site at the Dead Sea shore in Israel. J. Appl. Geophys. 64, 56–69. https://doi.org/10.1016/j.jappgeo.2007.12.003.

Ferrara, G., Tonarini, S., 1985. Radiometric geochronology in Tuscany: result and problems. Rend. Soc. It. Miner. Petrol. 40, 11–124.

Galve, J.P., Gutiérrez, F., Guerrero, J., Alonso, J., Ignacio, D., 2012. Application of risk, cost-benefit and acceptability analyses to identify the most appropriate geogrid solution to mitigate sinkhole damage on roads. Eng. Geol. 145-146, 65–77.

Griffin, W.P., 1949. Residual gravity in theory and practice. Geophysics 14, 39–56.

Guerrero, J., Gutiérrez, F., Lucha, P., 2004. Paleosubsidence and active subsidente due to evaporite dissolution in the Zaragoza area (Huerva River valley, NE Spain): processes, spatial distribution and protection measures for transport routes. Eng. Geol. 72, 309–329.

Intrieri, E., Gigli, G., Nocentini, M., Lombardi, L., Mugnai, F., Fidolini, F., Casagli, N., 2015. Sinkhole monitoring and early warning: an experimental and successful GB-InSAR application. Geomorphology 241, 304–314. https://doi.org/10.1016/j.geomorph.2015.04.018.

Intrieri, E., Fontanelli, K., Bardi, F., Marini, F., Carlà, T., Pazzi, V., Di Michele, F., Fanti, R., 2018. Definition of sinkhole triggers and susceptibility based on hydrogeomorphological analyses. Environ. Earth Sci. 77, 4. https://doi.org/10.1007/s12665-017-7179-3.

Kaufmann, G., 2014. Geophysical mapping of solution and collapse sinkholes. J. Appl. Geophys. 111, 271–288. https://doi.org/10.1016/j.jappgeo.2014.10.011.

Krawczyk, C.M., Polom, U., Trabs, S., Dahm, T., 2012. Sinkholes in the city of Hamburg - new urban shear-wave reflection seismic system enables high-resolution imaging of suberosion structures. J. Appl. Geophys. 78, 133–143. https://doi.org/10.1016/j.jappgeo.2011.02.003.

Lee, E.J., Shin, S.Y., Ko, B.C., Chang, C., 2016. Early sinkhole detection using a drone-based thermal camera image. Infrared Phys. Technol. 78, 223–232. https://doi.org/10.1016/j.infrared.2016.08.009.

Lotti, A., Saccorotti, G., Fiaschi, A., Matassoni, L., Gigli, G., Pazzi, V., Casagli, N., 2015. Seismic monitoring of rockslide: the Torgiovannetto quarry (Central Apennines, Italy). In: Lollino, G. (Ed.), Engineering Geology for Society and Territory. vol.2. Springer International Publishing, Switzerland, pp. 1537–1540. https://doi.org/10.1007/978-3-319-09057-3_272.

Lotti, A., Lazzeri, A.M., Beja, S., Pazzi, V., 2017. Could ambient vibration be related to *Cerithidea decollata* migration? Int. J. Geosci. 8, 286–295. https://doi.org/10.4236/ijg.2017.83013.

Maineri, C., Benvenuti, M., Costagliola, P., Dini, A., Lattanti, P., Ruggeri, G., Villa, I.M., 2003. Sericitic alteration at the La Crocetta deposits (Elba Island, Italy): interplay between magmatism, tectonic and hydrothermal activity. Mineral. Deposita 38, 6–86.

Martinez-Moreno, F.J., Pedrera, A., Ruano, P., Galindo-Zaldivar, J., Martos-Rosillo, S., Gonzalez-Castillo, L., Sanchez-Ubeda, J.P., Marin-Lechado, C., 2013. Combined microgravity, electrical resistivity tomography and induced polarization to detect deeply buried caves: algaidilla cave (Southern Spain). Eng. Geol. 162, 67–78. https://doi.org/10.1016/j.enggeo.2013.05.008.

Moritz, A., 1984. Geodetic reference system 1980. In: Tscherning (Ed.), The Geodesist's Handbook. C.C. Bulletin Geodesy. 58. pp. 388–398.

Nakamura, Y., 1989. A method for dynamic characteristics estimation of subsurface using microtremor on the ground surface. Q. Rep.Railw. Tech. Res. Inst. 30, 25–33.

Nettleton, L.L., 1942. Gravity and magnetic calculations. Geophysics 7, 293–310.

Pazzi, V., Morelli, S., Fidolini, F., Krymi, E., Casagli, N., Fanti, R., 2016a. Testing cost-effective methodologies for flood and seismic vulnerability assessment in communities of developing countries (Dajç northern Albania). In: Geomatics, Natural Hazards and Risk. 7. pp. 971–999. https://doi.org/10.1080/19475705.2015.1004374.

Pazzi, V., Morelli, S., Pratesi, F., Sodi, T., Valori, L., Gambacciani, L., Casagli, N., 2016b. Assessing the safety of schools affected by geo-hydrologic hazards: the geohazard safety classification (GSC). Int. J. Disaster Risk Reduction 15, 80–93. https://doi.org/10.1016/j.ijdrr.2015.11.006.

Pazzi, V., Tapete, D., Cappuccini, L., Fanti, R., 2016c. An electric and electromagnetic geophysical approach for subsurface investigation of anthropogenic mounds in an urban environment. Geomorphology 273, 335–347. https://doi.org/10.1016/j.geomorph.2016.07.035.

Pazzi, V., Lotti, A., Chiara, P., Lombardi, L., Nocentini, M., Casagli, N., 2017a. Monitoring of the vibration induced on the Arno masonry embankment wall by the conservation works after the May 25, 2016 riverbank landslide. Geoenviron. Disasters 4, 6. https://doi.org/10.1186/s40677-017-0072-2.

Pazzi, V., Tanteri, L., Bicocchi, G., D'Ambrosio, M., Caselli, A., Fanti, R., 2017b. H/V measurements as an effective tool for the reliable detection of landslide slip surfaces: case studies of Castagnola (La Spezia, Italy) and Roccalbegna (Grosseto, Italy). Phys. Chem. Earth 98, 136–153. https://doi.org/10.1016/j.pce.2016.10.014.

Pueyo Anchuela, O., Pocovi Juan, A., Casas-Sainz, A.M., Anson-Lopez, D., Gil-Garbi, H., 2013. Actual extension of sinkholes: considerations about geophysical, geomorphological, and field inspection techniques in urban palnning projects in the Ebro basin (NE Spain). Geomorphology 189, 135–149. https://doi.org/10.1016/j.geomorph.2013.01.024.

Rocchi, S., Westerman, D.S., Dini, A., Innocenti, F., Tonarini, S., 2002. Two-stage growth of laccoliths at Elba Island, Italy. Geology 30, 938–986.

Samyn, K., Mathieu, F., Bitri, A., Nachbaur, A., Closset, L., 2014. Integrated geophysical approach in assessing karst presence and sinkhole susceptibility along flood-protection dykes of the Loire River, Orléans, France. Eng. Geol. 183, 170–184. https://doi.org/10.1016/j.enggeo.2014.10.013.

Santarato, G., Ranieri, G., Occhi, M., Morelli, G., Fischanger, F., Gualerzi, D., 2011. Three-dimensional electrical resistivity tomography to control the injection of expanding resins for the treatment and stabilization of foundation soils. Eng. Geol. 119, 18–30. https://doi.org/10.1016/j.enggeo.2011.01.009.

SESAME, 2004. Guidelines for the implementation of the H/V spectral ratio technique on ambient vibrations. In: Measurements, processing and interpretation. SESAME European research project, WP12 – deliverable D23.12. European Commission – Research General Directorate (Project No. EVG1-CT-2000-00026 SESAME).

Sevil, J., Gutiérrez, F., Zarroca, M., Desir, G., Carbonel, D., Guerrero, J., Linares, R., Roqué, C., Fabregat, I., 2017. Sinkhole investigation in an urban area by trenching in combination with GPR, ERT and high-precision leveling. Mantled evaporite karst of Zaragoza city, NE Spain. Eng. Geol. 231, 9–20.

Sgarlato, G., Lombardo, G., Rigano, R., 2011. Evaluation of seismic site response nearby underground cavities using earthquake and ambient noise recordings: a case study in Catania area, Italy. Eng. Geol. 122, 281–291. https://doi.org/10.1016/j.enggeo.2011.06.002.

Smith, D.L., 1986. Application of the pole-dipole resistivity technique to the detection of solution cavities beneath highways. Geophysics 51, 833–837.

Viero, A., Galgaro, A., Morelli, G., Breda, A., Francese, R.G., 2015. Investigations on the structural setting of a landslide-prone slope by means of three-dimensional electrical resistivity tomography. Nat. Hazards 78, 1369–1385. https://doi.org/10.1007/s11069-015-1777-8.

Waltham, T., Bell, F., Culshaw, M., 2005. Sinkholes and Subsidence – Karst and Cavernous Rocks in Engineering and Construction. Springer Verlag, Berlin Heidelberg, New York.

Zhou, W., Beck, B.F., Adams, A.L., 2002. Effective electrode array in mapping karst hazards in electrical resistivity tomography. Environ. Geol. 42, 922–928. https://doi.org/10.1007/s00254-002-0594-z.

Zini, L., Calligaris, C., Forte, E., Petronio, L., Zavagno, E., Boccali, C., Cucchi, F., 2015. A multidisciplinary approach in sinkhole analysis: the Quinis village case study (NE-Italy). Eng. Geol. 197, 132–144. https://doi.org/10.1016/j.enggeo.2015.07.004.